Edelweiss Applied Science and Technology
ISSN: 2576-8484
Vol. 8, No. 6, 413-430
2024
Publisher: Learning Gate
DOI: 10.55214/25768484.v8i6.2093

First-principle investigation of stability, magnetic moments, electronic and optical properties of Fe with GGA and GGA+U

Yousif Shoaib Mohammed[1,2*], Ahmed Faisal Alhag[1], Anas Ramadan[3]
[1]Department of Physics, College of Science, Qassim University (Buraidah, Saudi Arabia); ys.idris@qu.edu.sa (Y.S.M.); af.alhaj@qu.edu.sa (A.F.A.).
[2]Department of Science, Karary University (PortSudan, Sudan).
[3]Key Laboratory of Polymer Materials of Gansu Province, College of Chemistry and Chemical Engineering, Northwest Normal University (Lanzhou, China); arm24730@gmail.com (A.R.).

Abstract: The stability of the bcc FM of Fe, the magnetic moments, electronic structure, and optical properties have calculated for the cases of bcc and fcc Fe, for non-magnetic (NM), ferromagnetic (FM), and antiferromagnetic (AFM) states, using the full-potential linearized augmented plane wave method (FP-LAPW) with the generalized gradient approximation (GGA) and GGA+*U* within the framework of density functional theory (DFT), as implemented in the WIEN2k code. The magnetic moments increase when significant correlations are taken into account. The Density of State (DOS) changes significantly with the FM state but not much with the NM or AFM states, which is consistent with Iota's findings. The optical properties results obtained for the interband dielectric function $\varepsilon(\omega)$, variation in the energy-loss spectrum $L(\omega)$, absorption coefficient $\alpha(\omega)$, refractive index $n(\omega)$, reflectivity $R(\omega)$, and optical absorption $\sigma(\omega)$, are comparable with other studies. Our findings are in good agreement with earlier experimental and theoretical Findings.

Keywords: *DFT, Electronic structure, Fe, GGA & GGA+U, Optical properties, Stability.*

1. Introduction

In solid-state physics, one of the most fundamental concerns is the stability, optical, and magnetic properties of 3d transition elements. For a better understanding of the nature of these metals' electronic, optical, and magnetic characteristics in ambient settings, a great deal of theoretical and experimental research has been conducted (1–5). For elemental bcc vanadium, chromium, manganese, and iron, the transition from nonmagnetic to ferromagnetic behavior has been investigated (4) through the analysis of self-consistent parameter-free total-energy band-structure calculations in the local spin-density approximation using a fixed-spin-moment technique. In our earlier work (5), we used the Vienna ab initio Simulation Package (VASP) to investigate the stability of ferromagnetism in Fe, Co, and Ni metals at high pressure with GGA and GGA+*U*. Using XAS and XMCD spectroscopies, R. Torchio et al. (6) investigated the characteristics of materials at high pressure. Examining the relationship between structure and magnetism in 3D metals enables the replication of the physical environments of unreachable areas of Earth and planets. In addition, density functional theory (DFT) first-principles simulations were used to examine the magnetic, structural, and energetic features of bulk Fe and Cr (7). Additionally, the Fermi-surface, optical, and photoemission properties of copper have been described using self-consistent band theory (8). A review has been done on the magnetic characteristics of Fe, Co, and Ni transition-metal nanowire arrays made via electro-deposition (1).

In this work, we have used the WIEN2k code to perform GGA and GGA+U computations to investigate the stability, DOS, magnetic, and optical properties of bcc and fcc Fe (9). A theory type that

* Correspondence: ys.idris@qu.edu.sa

can reconcile the itinerant- and localized-electron models of a ferromagnetic metal is discussed in the context of iron magnetism (10). Through the computation of the total electronic band-structure energy for four distinct spin configurations, the magnetism in iron at high temperature is examined (11).

From experimental perspective, the characteristics of 3d transition metals have been extensively studied through a variety of methodologies from an experimental perspective. Boulard, E. et al. (12) experimentally demonstrated stability of Fe-rich carbonates at temperatures of 1450-3600 K and pressures of 40 to 105 GPa, which correspond to depths of approximately 1000–2400 km in the Earth's lower mantle. Additionally, metallography, electron-probe microanalysis (EPMA), x-ray diffraction (XRD), and differential thermal analysis (DTA) were used to redetermine the phase diagram of the binary Fe-Zr system across the complete composition range (13). Furthermore, thermal analysis was used to conduct experimental research on the Fe-Pr and Fe-Nd alloys (14). In the binary systems of Fe-Pr and Fe-Nd, the temperatures of the invariant reactions and liquidus were measured. Using spectroscopic ellipsometry, the optical and magneto-optical characteristics of Fe nanoparticles embedded in amorphous Al2O3 with diameters ranging from 2 to 8 nm are investigated as a function of their size and shape (15).

Moreover, the growth of a single crystal from a melt using a modified vertical gradient freeze approach, followed by high-temperature treatment to remove free charge carriers, was also described as a methodology for producing high-quality single-crystal active elements for a Fe:CdTe laser (16). The general equivalence of the classical magneto-optical formalism dielectric tensor! and the resonant atomic scattering factor in the electric dipole approximation is demonstrated in describing pure charge contributions as well as first- and second-order magnetic contributions, while the properties of Fe are taken into consideration across its 2p core levels (17).

From theoretical perspective, Tiago M. L. et al (18) examine, the evolution of the magnetic moment in iron clusters with 20–400 atoms, using numerical calculations from fundamental principles based on real-space pseudopotentials and density-functional theory. As the clusters get closer to the bulk limit, they discovered an overall drop in magnetic moment. Additionally, computer simulation is used to study the finite-temperature magnetic characteristics of iron thin films across a wide temperature range, up to the ferromagnetic-paramagnetic phase transition (19). Using a novel form of synchrotron radiation three-dimensional x-ray microscopy, K Schlage et al. (20) have tracked the self-assembly of a magnetic antidot array during Fe sputter deposition onto a highly ordered, nanostructured polymer template. Additionally, the magnetism and phase transition of iron under pressure are studied by Zeng, Z. et al. (21) utilizing the spin-polarized generalized gradient approximation within the plane-wave pseudopotential density functional theory. They discovered that the body-centered-cubic (bcc) ferromagnetic ground state of iron exists.

In terms of optical characteristics, JH Weaver et al. (22) investigated the metallic elements' optical characteristics in 3d, 4d, and 5d transition metals. The effects of iron (II) and iron (III) on the ultraviolet and visible (UV-vis) absorption and fluorescence of solutions comprising two assessments of dissolved organic matter (DOM) fractions and two surface water samples have been reported by Brett A. Poulin et al. (23). Moreover, the energy values and wave functions found by the APW approach in the energy range of 0–40 eV are used to calculate the complex dielectric function $\varepsilon(0, \omega)$ and energy-loss function-$\mathrm{Im}[\varepsilon(0, \omega)^{-1}]$ of the 3d transition metals (V, Cr, Fe, and Ni) within RPA (24).

Conversely, the structural, electrical, magnetic, and optical characteristics of the Fe6 cluster adsorbed on the surface of a boron nitride sheet are investigated through the application of ab initio density functional theory (25). They discovered that there are tiny magnetic moments in the boron and nitrogen atoms of the boron nitride sheet surrounding the Fe cluster. In a different study, S. Dadashi et al. (26) investigated the effect of pure iron by creating iron oxide nanoparticles in deionized water and acetone using pulsed laser ablation. During ablation, the pure iron target was manually rotated. Scanning electron microscopy (SEM), X-ray diffraction (XRD), and UV-visible spectroscopy were used to analyze the particle size and shape, crystal structure, and optical properties of the nanoparticles, respectively.

Edelweiss Applied Science and Technology
ISSN: 2576-8484
Vol. 8, No. 6: 413-430, 2024
DOI: 10.55214/25768484.v8i6.2093

2. Methods

The full-potential linearized augmented plane wave (FP-LAPW) approach (27, 28) was utilized for all calculations in this work. It is based on density functional theory (DFT) (29, 30), and it is implemented in the WIEN2k computational package code (9, 31, 32). Ground state energy, optical properties, and the DOS for different Iron (Fe) states per formula unit for each of the bcc and fcc phases in NM, FM, and AFM states were calculated using FP-LAPW. We utilized a (1×1×1) supercell with space group (47_Pmmm) for fcc and a (1×1×1) supercell with space group (221_Pm_3m) for bcc in order to perform AFM calculations.

For each case, the parameterization technique developed by Perdew-Burke-Ernzerhof (PBE) (33, 34) included the exchange correlation interaction under Generalized Gradient Approximation (GGA). In the atomic sphere, the wave function is expanded into atomic-like functions (radial functions times spherical harmonics), and in the interstitial area, it takes the form of a plane wave basis. The experimental band gap is known to be underestimated by the GGA-PBE for strongly correlated systems (35).

We use a rotationally invariant version of DFT+U, as suggested by Dudarev et al. (36, 37), to account for the electronic correlation. Here, the on-site Coulomb interaction energy and the exchange energy are denoted by the parameters U and J, respectively. Due to the fact that only the difference between U and J is deemed significant, the parameters U and J were not employed independently. Reference (38) provides the GGA+U's details. We utilize (U-J) = 2.3 eV, given from (5, 39), in GGA+U calculations for our bcc and fcc Fe, where the exchange energy parameter is set to the standard value of J=1 eV. Brillouin zone sampling makes use of the Monkhorst-Pack technique (40). The irreducible Brillouin zone has 1000 k points, and given a well-converged set of findings, $R_{MT}\times K_{max}$=8.00, where K_{max} is the plane wave cut-off. G_{max}, whose value is assumed to be 12.00, indicates the magnitude of the highest wave vector in charge density. In subsequent iterations, the cut-off energy and charge convergence criterion is up to 0.0001e charge (41). Blochl corrections were applied while utilizing the linear tetrahedron approach for integration across the Brillion zone in total energy and DOS computations (42, 43).

The Murnaghan equations of state (EOS) (44 – 46) were fitted to the computed total energy per unit cell as a function of unit cell volume to get the equilibrium volume V_o, the zero-pressure bulk modulus B_o and its pressure derivatives B'_o, and the magnetic moments of the states.

3. Results and Discussion

3.1. Strucure and Magnetic Properties

The computed total energy (atomic energy) for the bcc and fcc of Fe metal for the NM, FM, and AM phases with the GGA and GGA+U, respectively, is displayed as a function of volume in Figuer 1. We deduced from this figure that the ground state of the Fe atom is ferromagnetic bcc for both GGA and GGA+U computations. Our findings corroborated those of other work (3, 5, 47). The GGA and GGA+U computations indicate that. For each phase, Table 1 displays the calculated equilibrium atomic energy E, lattice constant a, and atomic volume V_o at equilibrium volume. We confirmed from this table that the ground state of the Fe is an FM bcc structure, as anticipated by our GGA and GGA+U computations, accurately forecasted that the Fe's ground state has an FM bcc structure in line with the conclusions of previous studies (48, 49).

Edelweiss Applied Science and Technology
ISSN: 2576-8484
Vol. 8, No. 6: 413-430, 2024
DOI: 10.55214/25768484.v8i6.2093

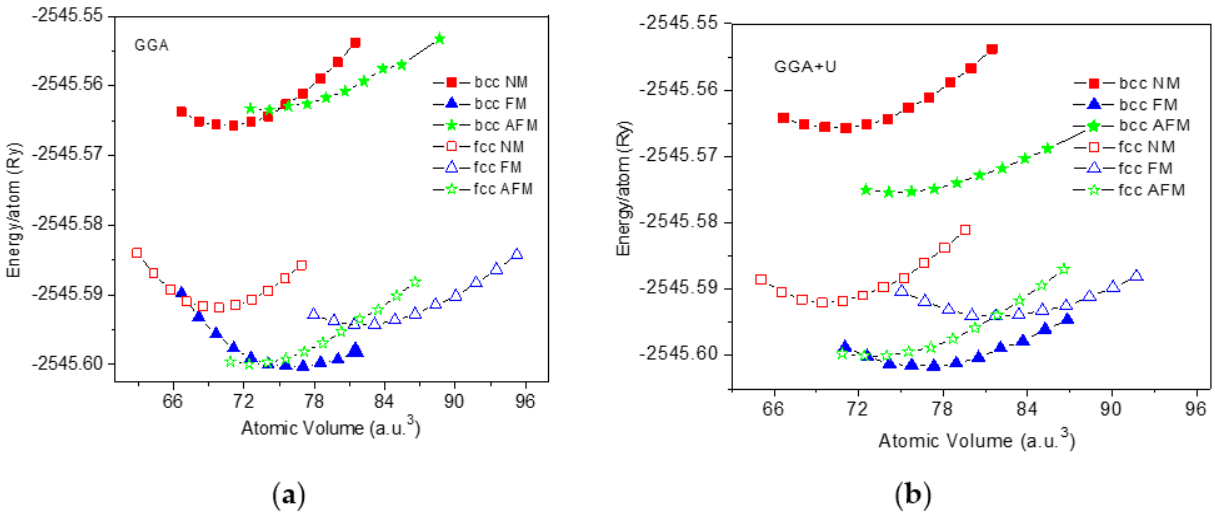

Figure 1.
(Online colour) Calculated total energies as a function of the atomic volume for Fe with Murnaghan EOS; solid symbols for bcc and open symbols for fcc, square for NM, Triangle for FM and star for AFM with (a) GGA and (b) GGA+*U*.

Table 1 showed that the atomic volumes for Fe's bcc and fcc alter oscillatorily when strong correlations are taken into account. This table also makes it evident that, when compared to other earlier work (50 – 52), such as our earlier study (5) on the stability of ferromagnetism in Fe, Co, and Ni metals at high pressure with GGA and GGA+*U*, our results are fairly plausible.

Table 1.
Displays the computed values of the lattice constant a, atomic volume V_0, and atomic energy E for the NM, FM, and AFM states in the bcc and fcc Fe phases with Murnaghan EOS, respectively, together with the findings of earlier calculations and experimental data (the GGA+*U* calculations' results are in parenthesis).

Metal	*a (A°)*	*V_o(Å^3)*	*E (Ry)*	Reference
bcc Fe NM	2.754(2.751)	10.44(10.41)	-2545.5658 (-2545.5658)	This work
	2.76	10.52	-2545.5754	(50)
bcc Fe FM	2.827(2.828)	11.29(11.31)	-2545.6003 (-2545.6016)	This work
	2.84	11.40	-2545.6107	(50)
	2.83	11.33		(53)
Exp	2.87	11.82		(51)
Exp	2.866	11.78		(54)
bcc Fe AFM	2.796(2.807)	10.92(11.05)	-2545.5634 (-2545.5754)	This work
fcc Fe NM	3.4564(3.4563)	10.32(10.32)	-2545.5919 (-2545.5920)	This work
	3.45	10.30	-2545.5908	(50)
fcc Fe FM	3.649(3.646)	12.14(12.12)	-2545.5943 (-2545.5941)	This work
	3.63	11.97	-2545.5902	(50)
	3.447	10.24		(50)
fcc Fe AFM	3.505(3.511)	10.76(10.82)	-2545.6000 (-2545.6001)	This work

Edelweiss Applied Science and Technology
ISSN: 2576-8484
Vol. 8, No. 6: 413-430, 2024
DOI: 10.55214/25768484.v8i6.2093

	3.376	10.13	-2541.2000	(55)

Table 2 lists the ground-state parameters, known experimental data, and prior all-electron computations, together with the zero-pressure bulk modulus B_0, its pressure derivative B'_0, equilibrium volume V_0, and the magnetic moments (μ). Table 2 demonstrates that the magnetic moments rise with the inclusion of strong correlations. Furthermore, as can be observed from this table, the GGA computations produce findings that are rather realistic when compared to other results (53, 56 – 58). As a result, the GGA results exhibit improved agreement with experiments and other theoretical investigations, which is a significant advance above previous DFT results.

Table 2.
Displays the computed values of the atomic volume V_0, bulk modulus B_0, bulk modulus pressure derivative B'_0, and the magnetic moments (μ) for the NM, FM, and AFM states of bcc and fcc Fe, respectively, as well as previous calculated results and experimental data (the GGA+U calculations' results are in parenthesis).

Metal	*a (A°)*	*V_0(Å^3)*	*E (Ry)*	*B_0 (GPa)*	*B_0'*	*M (μB)*	Reference
bcc Fe NM	DFT	GGA (GGA+U)	10.44 (10.41)	259.9 (235.8)	4.02 (2.61)		This work
	DFT	GGA	10.18	267			(53)
bcc Fe FM	DFT	GGA (GGA+U)	11.29 (11.31)	196.7 (199.9)	5.19 (6.59)	2.23 (2.44)	This work
	FLAPW	GGA	11.94	182		2.13	(59)
	DFT	GGA (GGA+U)	11.33 (12.32)			2.18 (2.73)	(60)
	LCAO	GGA	11.94	174		2.20	(61)
	LAPW	GGA	11.70	169		2.32	(62)
	DFT	LDU+U	12.58	212		2.60	[63]
	DFT	GGA (GGA+U)	11.80 (10.87)	168.8 (168.3)	3.68 (4.40)	2.23 (2.76)	[5]
	DFT		11.44	177.9	5.09		(52)
	PAW		11.46	188		2.21	(64)
		Exp	11.80	168		2.22	(56)
		Exp	11.78	172	5.00		(54)
bcc Fe AFM	DFT	GGA (GGA+U)	10.92 (11.05)	155.7 (194)	6.62 (8.93)	-0.75 (-0.14)	This work
	PAW	GGA	10.58	166		1.22	(53)
fcc Fe NM	DFT	GGA (GGA+U)	10.32 (10.32)	293.2 (293.9)	4.47 (4.84)		This work
	DFT	GGA	10.30	282			(53)
fcc Fe FM	DFT	GGA (GGA+U)	12.14 (12.12)	192.8 (176.5)	5.83 (4.00)	2.71 (2.67)	This work
	FLAPW	GGA				2.637	(57)
	DFT	GGA	10.27	282			(53)
fcc Fe AFM	DFT	GGA (GGA+U)	10.76 (10.82)	238.4 (209.3)	9.47 (4.22)	-0.074 (0.167)	This work
	DFT	GGA	10.39	198		1.23	(53)
		Exp	10.63			0.70 (65)	(58)

Edelweiss Applied Science and Technology
ISSN: 2576-8484
Vol. 8, No. 6: 413-430, 2024
DOI: 10.55214/25768484.v8i6.2093

3.2. Electronic Properties

As illustrated in Figuers 2 and 3, we report the total densities of states (TDOS) and partial densities of states (PDOS) for various phases of NM, FM, and AFM using GGA and GGA+*U* calculations, respectively, to explore the effect of states on the electronic structure, which explains energy levels of bcc and fcc Fe. The computations have been recorded between -7 and 7 eV of energy. The vertical dotted line in our calculated DOS denotes the Fermi level or energy. Figure 2 shows that, for both GGA and GGA+*U* computations, the DOS changes significantly with the FM state but not much with the NM or AFM states, which is consistent with Iota's experiments (1) and pertinent theoretical research (5, 24). Additionally, we can observe that for AFM bcc Fe, the DOS at the Fermi level is maximum; conversely, for fcc Fe, it turns highest for NM instances. Table 3 shows that for both GGA and GGA+U computations, the DOS at Fermi level is smaller for FM bcc and fcc. The Stoner requirement for an itinerant is known to be $N(E_F)I>1$, where I is the Stoner parameter and $N(E_F)$ is the DOS at the Fermi level (E_F) for both GGA and GGA+*U* computations. The condition is evidently met for both bcc and fcc NM and AFM states, but $N(E_F)I<1$ indicates a stable state in the FM case. Additionally, Figure 2 revealed that the e_g level is the primary contributor to the Fermi level of NM and AFM. Furthermore, it can be comprehended by taking into account the addition of *U* and *J*, which results in contributions to the Stoner parameter, I (38).

Table 3.
Displays the computed values of DOS at Fermi energy EF for NM, FM, and AFM states of bcc and fcc Fe by GGA and GGA+U (the GGA+*U* calculations' results are in parenthesis).

Case	bcc	fcc
NM	2.426(2.527)	2.860(4.180)
FM	0.798(0.289)	0.214(0.113)
AFM	2.936(3.344)	1.842(1.942)

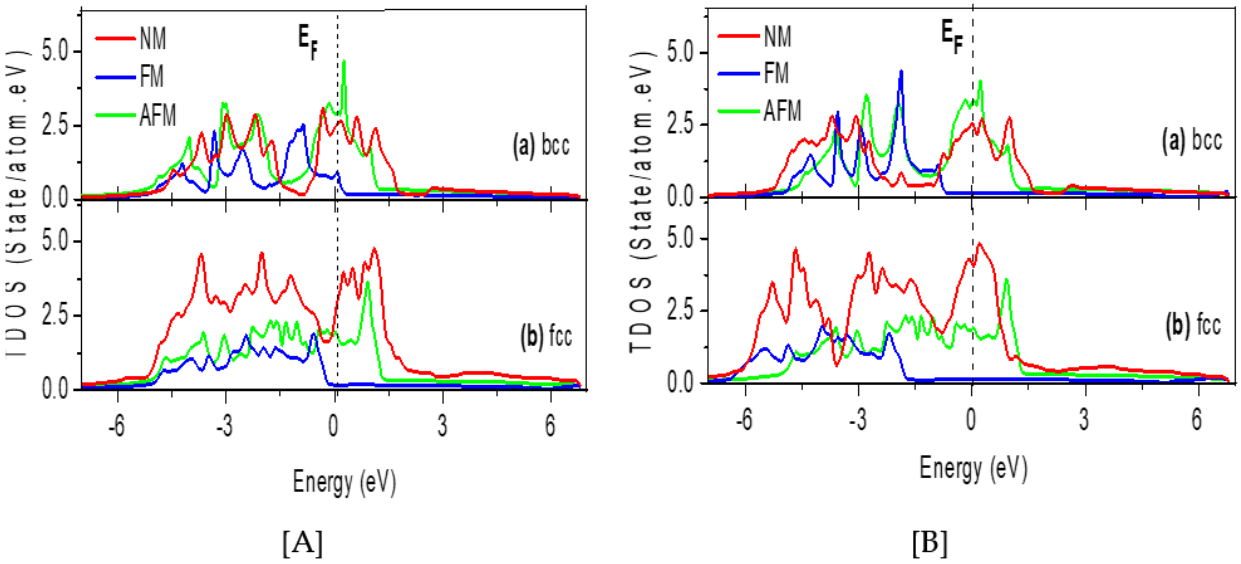

Figure 2.
(Online colour) Calculated TDOS of NM, FM and AFM states for Fe, red for NM, blue for FM and green for AFM, (a) bcc, (b) fcc, [A] GGA and [B] GGA+*U*.

Figures 3 and 4 displayed the PDOS of tot, s, and d orbitals for NM, FM, and AFM states for bcc and fcc Fe with GGA and GGA+*U*, respectively. One antiferromagnetic state eliminates the instability

caused by the high density of states at the Fermi energy; this outcome is in great agreement with that stated in Ref (66).

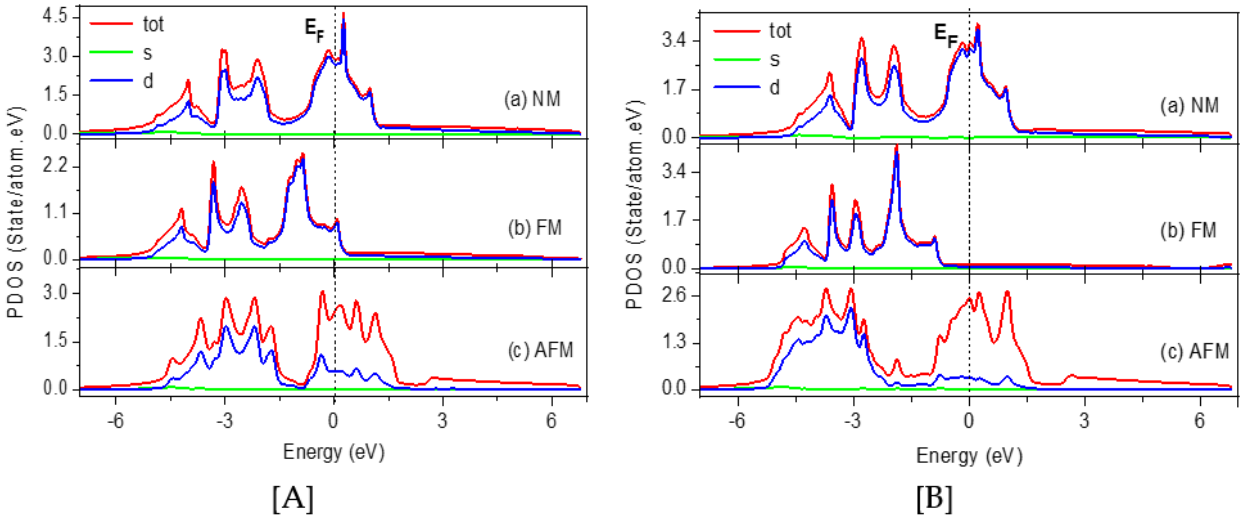

Figure 3.
(Online colour) Calculated PDOS for bcc Fe, red for total, green for s and blue for d DOS, (a) NM, (b) FM, (c) AFM, [A] GGA and [B] GGA+*U*.

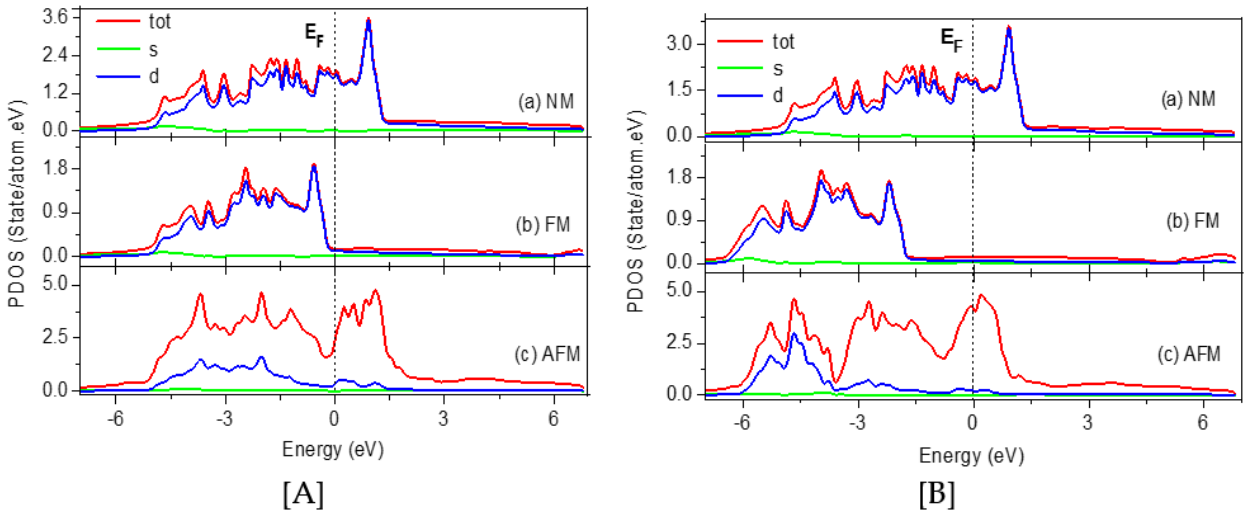

Figure 4.
(Online colour) Calculated PDOS for fcc Fe, Red for total, Green for s and Blue for d DOS, (a) NM, (b) FM, (c) AFM, [A] GGA and [B] GGA+*U*.

Table 4 illustrates how the band layers with the highest energy levels for PDOS are positioned in each of our situations. The level Fe:3d is the primary source of these pecks. Additionally, it is evident from Figures 3 and 4 that the d orbital produces the greatest density of state. We see that, for the cases under investigation, Fe d-states contribute to the valence band maximum (VBM) with the least effect for Fe s and f-states, which is consistent with the findings of Cococcioni M et al. (63).

Edelweiss Applied Science and Technology
ISSN: 2576-8484
Vol. 8, No. 6: 413-430, 2024
DOI: 10.55214/25768484.v8i6.2093

Table 4.
Displays the computed position of the highest level in energy of the band layers for NM, FM and AFM states of bcc and fcc Fe by GGA and GGA+*U*, (the GGA+*U* calculations' results are in parenthesis).

Case	bcc	fcc
NM	0.249,4.563 (0.233,3.978)	0.933,3.530 (0.933,3.593)
FM	-0.848,2.510 (-0.585,1.853)	-1.821,4.259 (-3.912,1.936)
AFM	-0.322,3.068 (0.981,2.775)	1.126,4.687 (0.175,4.785)

Furthermore, PDOS plots illustrate the p-d hybridization. By contrasting the distribution of DOS under GGA and GGA+U, it is clear that the Hubbard term alters the local position of states. As can be shown in Table 4 and Figuer 5 at the maximum energy level of the band layers, the addition of U caused a downward shift of the Fe states, which lessens the hybridization of the Fe 3d. For NM and AFM, the impurity states close to the Fermi level essentially stay the same, while the FM calculation appears to be different, with the lowest energy at the Fermi level for both GGA and GGA+U. The data shown in Figure 2 indicates that the DOS at E_F is maximum for bcc AFM and fcc NM, and minimum for bcc and fcc FM, respectively.

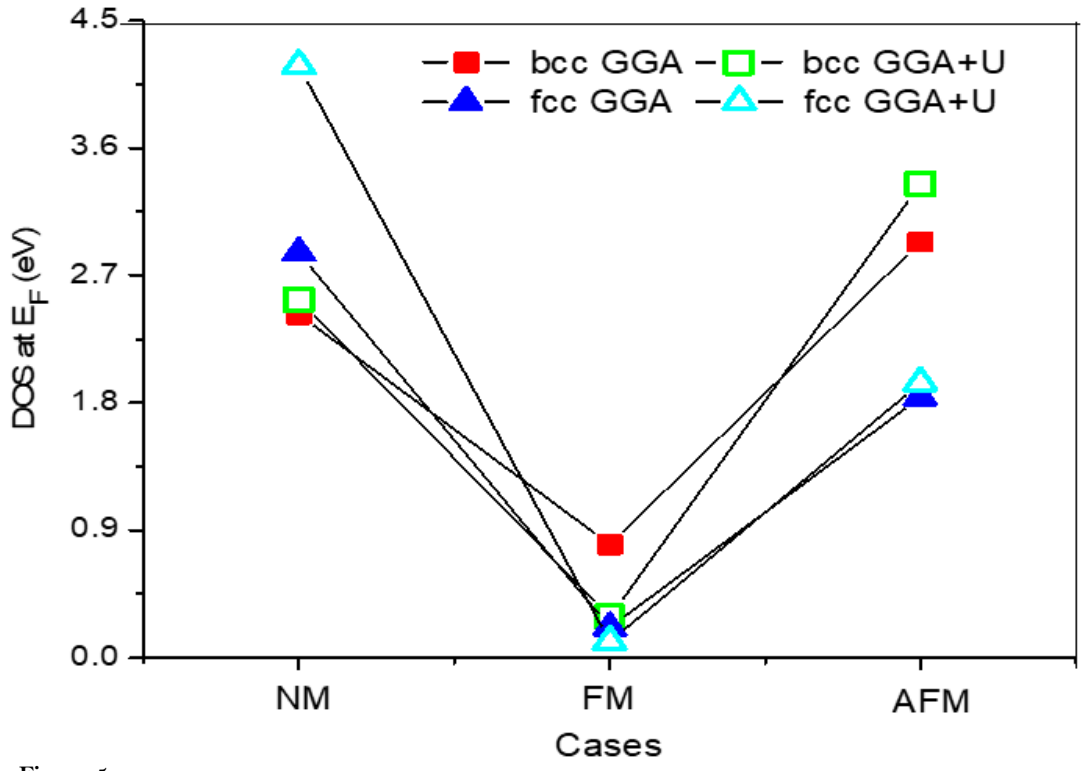

Figure 5.
(Online colour) Calculated DOS at EF of bcc square and fcc tringle solid symbols for GGA and open symbols for GGA+*U*.

3.3. Optical Properties

Among the most significant characteristics of materials that have been studied are their optical properties (24). The band structures that the inter/intra-band transitions describe have a close relationship with the optical properties. The optical response of a material is thought to be the interaction of the incident photon with the atoms, and it is represented by the dielectric function $\varepsilon(\omega)$. When a crystal has a cubic symmetry structure, it is said to be isotropic ($\varepsilon=\varepsilon_{xx}=\varepsilon_{yy}=\varepsilon_{zz}$). It is known that

Edelweiss Applied Science and Technology
ISSN: 2576-8484
Vol. 8, No. 6: 413-430, 2024
DOI: 10.55214/25768484.v8i6.2093

the interband dielectric function can be used to determine the physical characteristics of solids and to characterize the optical response of the medium at all photon energy. It is a complex function that is given as (67).

$$\varepsilon(\omega) = \varepsilon_1(\omega) + i\varepsilon_2(\omega) \quad [1]$$

Where ω is the incident photon frequency, that described the absorptive behavior by the real part $\varepsilon_1(\omega)$ and imaginary one $\varepsilon_2(\omega)$ of the complex dielectric function, which are directly related to the electronic band structure. Furthermore, and are subject to the Kramers-Kronig relation (68).

$$\varepsilon_1(\omega) = 1 + \frac{2}{\pi} P \int_0^{\infty} \frac{\omega' \varepsilon_2(\omega')}{(\omega'^2 - \omega^2)} d\omega' \quad [2]$$

$$\varepsilon_2(\omega) = \frac{2\omega}{\pi} P \int_0^{\infty} \frac{\varepsilon_1(\omega') - 1}{(\omega'^2 - \omega^2)} d\omega' \quad [3]$$

Here, P represents the Cauchy integral's principle value. Upon determining $\varepsilon_1(\omega)$ and $\varepsilon_2(\omega)$, all other optical parameters can be easily calculated; such as the absorption coefficient $\alpha(\omega)$, refractive indices $n(\omega)$, and energy loss function $L(\omega)$ (69 – 71).

The interband dielectric function $\varepsilon(\omega)$ calculated by FP-LAPW for NM, FM, and AFM states of bcc and fcc Fe for real part $\varepsilon_1(\omega)$ and imaginary part $\varepsilon_2(\omega)$ are displayed at Figures 6 and 7. In these figures, the values of the $\varepsilon_1(\omega)$ and $\varepsilon_2(\omega)$ for our cases are computed between 0 and 13 eV with GGA and GGA+U, respectively. Also, from these figures, we found that the behavior of our $\varepsilon_1(\omega)$ and $\varepsilon_2(\omega)$ is in good agreement with previous studies (72, 73). Again from figures 6 and 7, one can see that all peaks changed oscillatory with increasing energy with different numbers of peaks for any case, which is in line with the findings of earlier studies (24, 74).

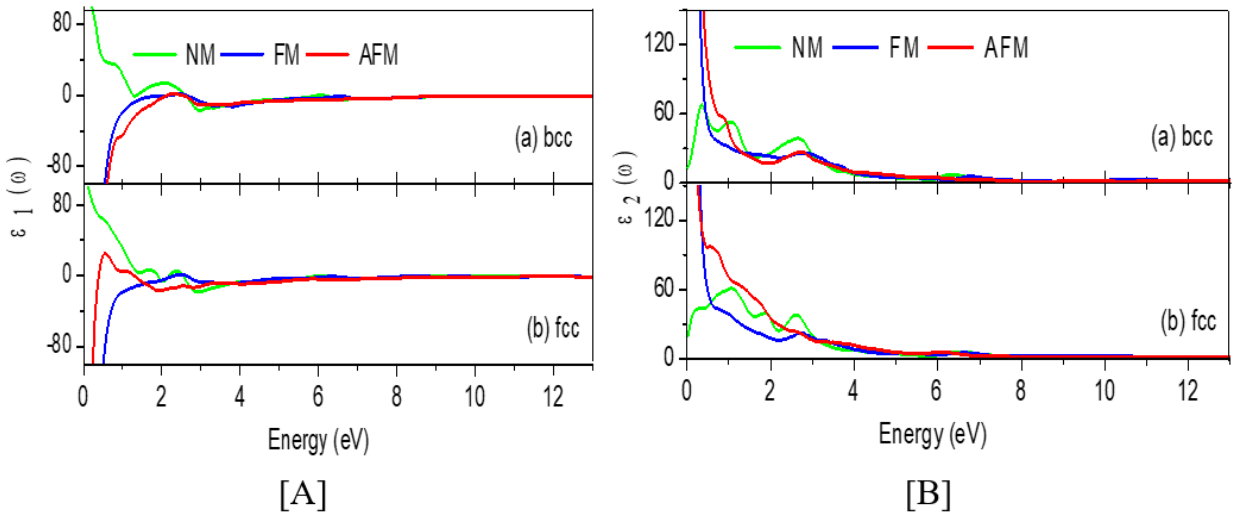

Figure 6.
(Online colour) Calculated the dielectric function of NM, FM and AFM states, between 0 and 13 eV for Fe (a) bcc, (b) fcc, [A] Real part $\varepsilon_1(\omega)$ and [B] Imaginary part $\varepsilon_2(\omega)$ with GGA.

Edelweiss Applied Science and Technology
ISSN: 2576-8484
Vol. 8, No. 6: 413-430, 2024
DOI: 10.55214/25768484.v8i6.2093

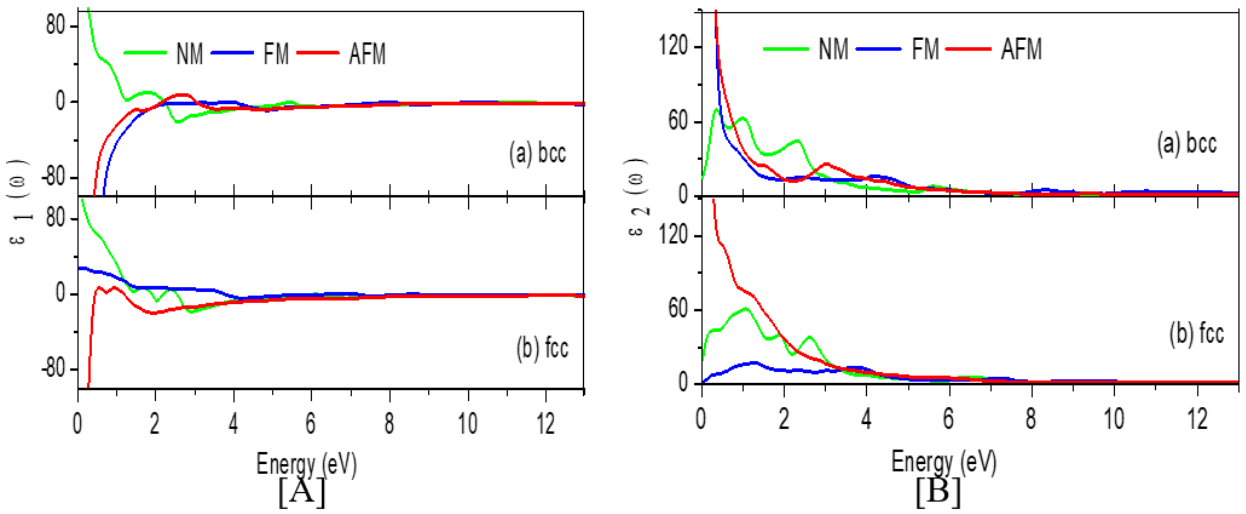

Figure 7.
(Online colour) Calculated the dielectric function of NM, FM and AFM states, between 0 and 13 eV for Fe (a) bcc, (b) fcc, [A] Real part $\varepsilon_1(\omega)$ and [B] Imaginary part $\varepsilon_2(\omega)$, with GGA+*U*.

The optical absorption coefficient and energy loss function were determined by first computing the imaginary and real parts of the dielectric function of Figures 6 and 7. The electron energy loss-spectrum $L(\omega)$ graph for the NM, FM, and AFM states with both GGA and GGA+*U* calculations as a function of photon energy is shown in Figure 8. An essential factor in defining elastic and non-scattering electron scattering (zero energy loss) is the energy loss function. According to (73), the electron excitations are mostly responsible for the energy losses at intermediate energies 0 –13 eV it is defined by:

$$L(\omega) = \varepsilon_2(\omega)/[\varepsilon_1^2(\omega) + \omega_2^2(\omega)] \quad [4]$$

For both the GGA and GGA+*U* calculations, the two significant groups of peaks occur in the energy range 4.00–13.00 eV; for the GGA and GGA+*U* calculations, the first group of peaks occurs at 5.00–7.00 eV and 4.00–9.00 eV, while for the second group, it occurs at 7.00–11.50 eV and 9.00–13.00 eV. For both GGA and GGA+U, the locations of the primary peaks in the energy range for the first and second groups are given in Table 5 (the GGA+*U* calculations are in [] square parenthesis). These figures and the graph's behavior match those of earlier studies (74). We have seen that the valley in optical conductivity, which represents electron scattering at that energy range, and the peaks in the energy loss function match. Our findings are in good accord with those of the earlier study (75).

Edelweiss Applied Science and Technology
ISSN: 2576-8484
Vol. 8, No. 6: 413-430, 2024
DOI: 10.55214/25768484.v8i6.2093

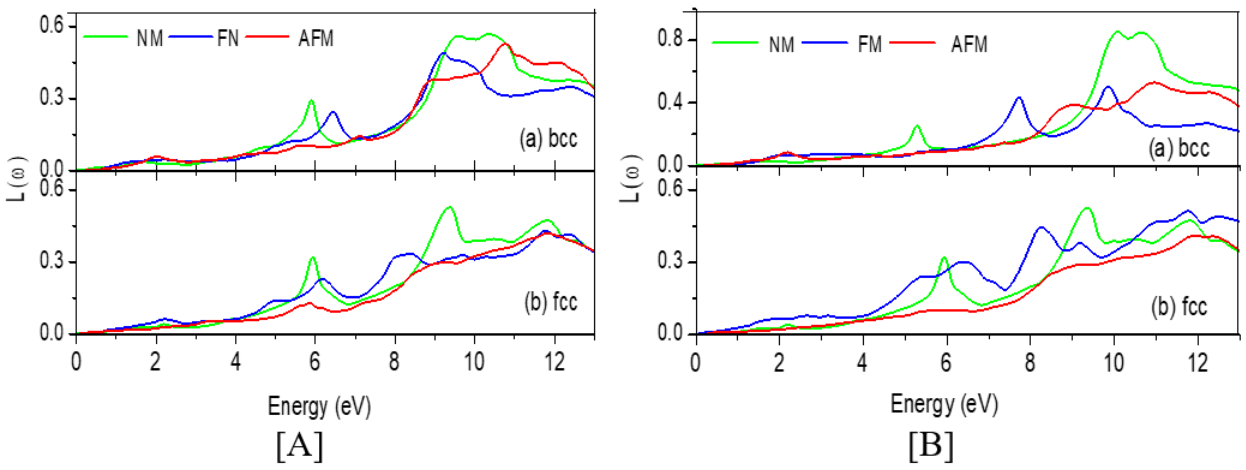

Figure 8.
(Online colour) Calculated energy loss function L(ω) of NM, FM and AFM states, between 0 and 13 eV for Fe (a) bcc, (b) fcc, [A] GGA and [B] GGA+*U*.

Table 5.
Displays the computed positions of the first and second peaks points of energy loss function for NM, FM and AFM states of bcc and fcc Fe by GGA and GGA+*U*, respectively. (the GGA+*U* calculations are in [] square parenthesis).

	Case	bcc	fcc
First peak	NM	(5.912,0.291) [5.295,0.244]	(5.912,0.310) [5.912,0.320]
	FM	(6.442,0.240) [7.766,0.432]	(6.177,0.229) [6.442,0.300]
	AFM	(5.691,0.108) [5.546,0.088]	(5.825,0.127) [5.912,0.117]
Second peak	NM	(9.622,0.566) [10.145,0.854]	(9.397,0.514) [9.397,0.524]
	FM	(9.221,0.484) [9.883,0.510]	(8.294,0.341) [8.338,0.443]
	AFM	(10.807,0.525) [8.911,0.400]	(9.131,0.310) [8.911,0.290]

Figure 9 shows the absorption coefficient $\alpha(\omega)$ for Fe crystals in bcc and fcc phases, calculated using Eq. [5], for NM, FM, and AFM using both GGA and GGA+*U* computations. The values range from 0 to 13 eV. The results for GGA+*U* are in parenthesis. Based on this figure, Table 6 lists the optical absorption active sites for NM, FM, and AFM with GGA and GGA+*U*, respectively. Table 6 and this figure's results demonstrate that, when using GGA calculations, the activation points for both bcc and fcc are higher. Additionally, Figure 9 demonstrates that, for both GGA and GGA+*U* computations, absorption rises with energy, which is consistent with findings from earlier study (74).

$$\alpha(\omega) = \sqrt{2\omega}\left[\sqrt{\varepsilon_1^2(\omega) + \varepsilon_2^2(\omega)} - \varepsilon_1(\omega)\right]^{1/2} \quad (5)$$

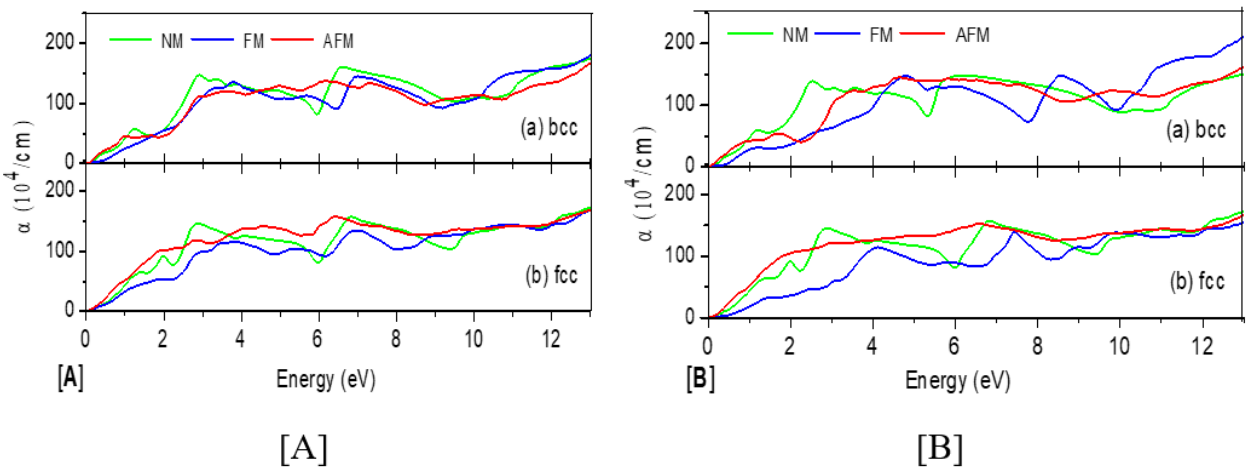

Figure 9.
(Online colour) Calculated absorption coefficient $\alpha(\omega)$ for Fe NM, FM and AFM states between 0 and 13 eV (a) bcc, (b) fcc, [A] GGA and [B] GGA+*U*.

Table 6.
Displays the computed activated points of absorption coefficient $\alpha(\omega)$ for Fe NM, FM and AFM states between 0 and 13 eV for bcc and fcc with GGA and GGA+*U*, (the GGA+*U* calculations' results are in parenthesis).

Case	bcc	fcc
NM	1.326 (1.237)	1.413 (1.368)
FM	2.251 (1.106)	1.854 (1.502)
AFM	1.016 (0.930)	0.930 (0.796)

The refractive index n(ω) is expressed in terms of $\varepsilon_1(\omega)$ and $\varepsilon_2(\omega)$, according to the relation.

$$n(\omega) = \left\{ \frac{\varepsilon_1(\omega)}{2} + \frac{\sqrt{\varepsilon_1^2(\omega)+\varepsilon_2^2(\omega)}}{2} \right\}^{1/2} \quad (6)$$

Figure 10 shows the variations in the refractive index n(ω) as a function of energy for the NM, FM, and AFM states of bcc and fcc Fe with GGA and GGA+U from 0 to 13 eV. A dimensionless number known as an optical medium's refractive index explains how a beam travel through it. According to the relation $n(\omega) = \sqrt{\varepsilon_r}$ of Mark Fox (76), there exists a link between the line morphologies of n(ω) spectra and those of ε1(ω). We can see from this figure that our findings agree with those of earlier work (15).

Edelweiss Applied Science and Technology
ISSN: 2576-8484
Vol. 8, No. 6: 413-430, 2024
DOI: 10.55214/25768484.v8i6.2093

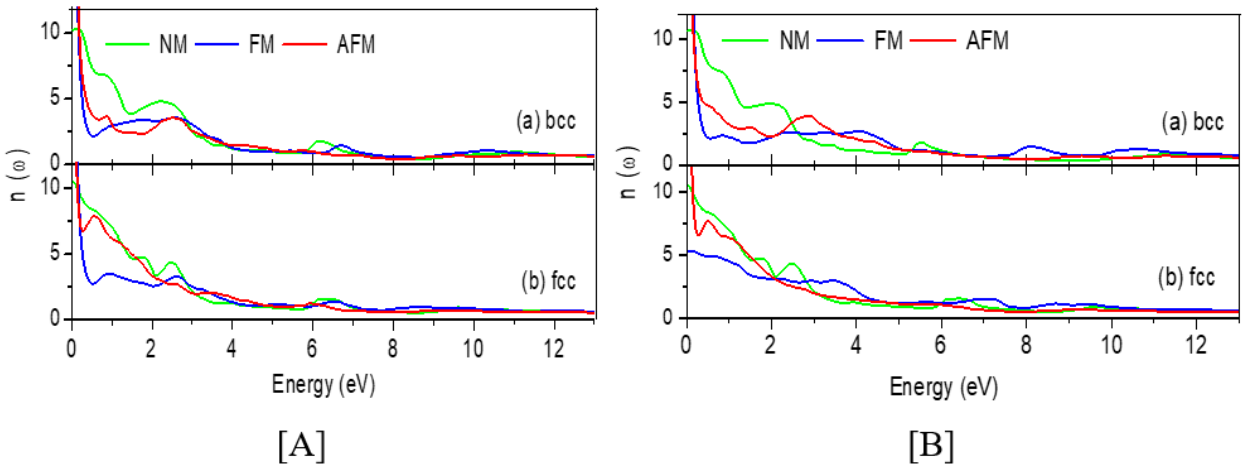

Figure 10.
(Online colour) Calculated the refractive index $n(\omega)$ for NM, FM and AFM states between 0 and 13 eV (a) bcc, (b) fcc, [A] GGA and [B] GGA+*U*.

The portion of energy that is reflected at the material interface is described by the reflection coefficient R(ω). It is provided by

$$R(\omega) = \left|\frac{\sqrt{\varepsilon(\omega)}-1}{\sqrt{\varepsilon(\omega)}+1}\right|^2 \qquad (7)$$

Figure 11 displays the variation in reflectivity $R(\omega)$ as a function of energy for NM, FM, and AFM of bcc and fcc Fe with GGA and GGA+*U* calculations at different states. This figure demonstrated how our findings behaved in line with previous research (73).

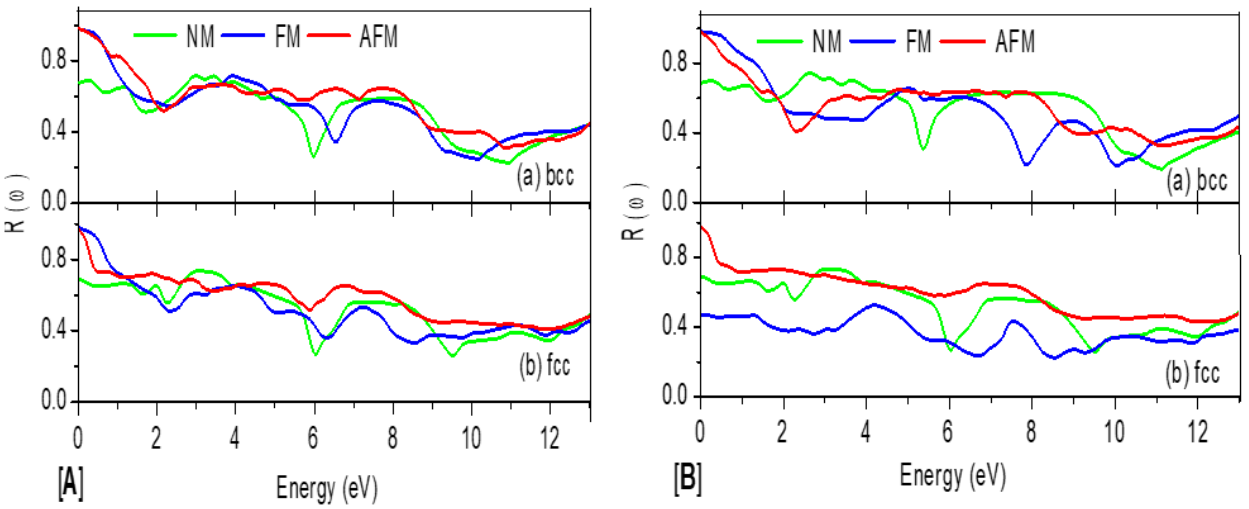

Figure 11.
(Online colour) Calculated reflectivity R(ω) for NM, FM and AFM states between 0 and 13 eV (a) bcc, (b) fcc, [A] GGA and [B] GGA+*U*.

Figures 12 and 13 display, respectively, the computed real portion $\sigma_1(\omega)$ and imaginary one $\sigma_2(\omega)$ of optical conductivity $\sigma(\omega)$ as a function of photon energy for NM, FM, and AFM states of bcc and fcc Fe

Edelweiss Applied Science and Technology
ISSN: 2576-8484
Vol. 8, No. 6: 413-430, 2024
DOI: 10.55214/25768484.v8i6.2093

with GGA and GGA+*U*. For all frequencies, the frequency-dependent dielectric function $\varepsilon(\omega)$ is related to the real part of the optical conductivity $Re[\sigma(\omega)]$. Our findings are consistent with earlier research (73).

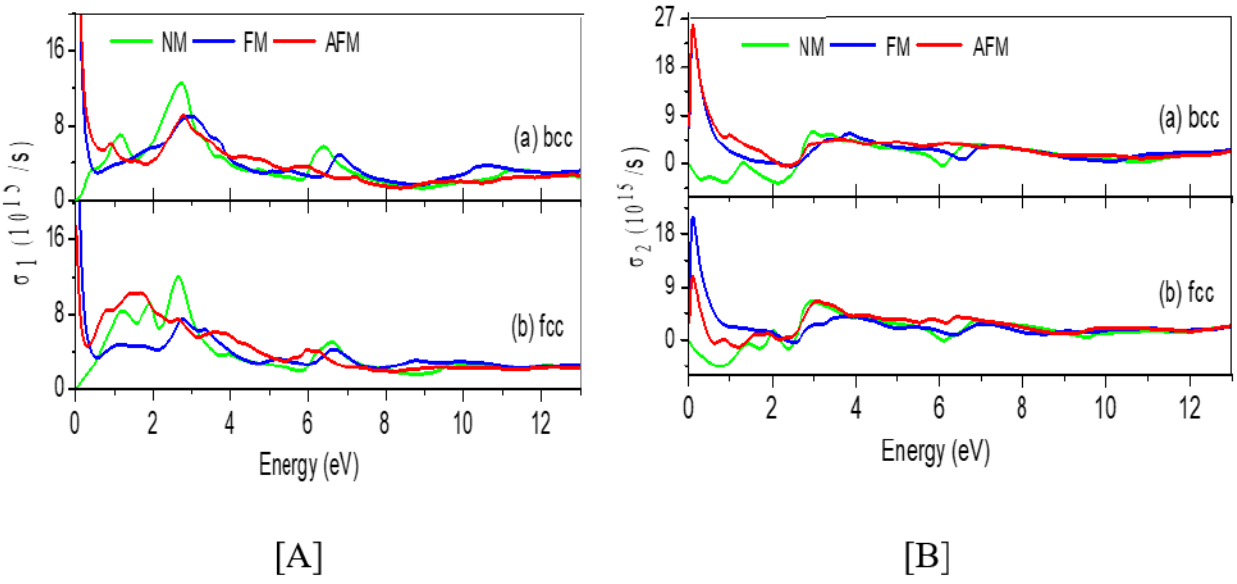

Figure 12.
(Online colour) The variation of optical conductivity for NM, FM and AFM states between 0 and 13 eV (a) bcc, (b) fcc, [A] real part $\sigma_1(\omega)$ and [B] imaginary part $\sigma_2(\omega)$ with GGA.

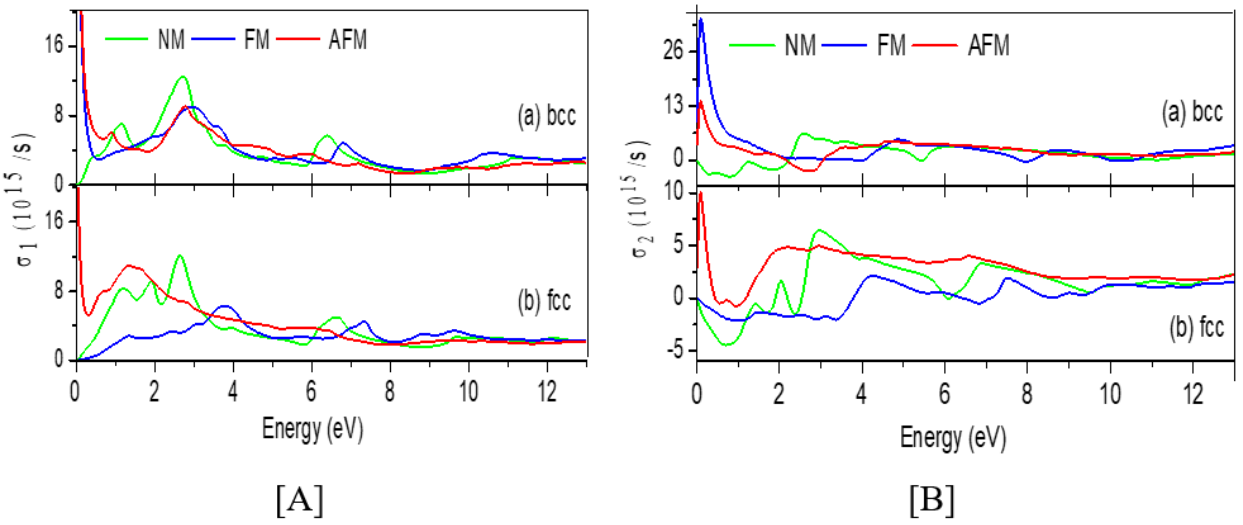

Figure 13.
(Online colour) The variation of optical conductivity for NM, FM and AFM states between 0 and 13 eV (a) bcc, (b) fcc, [A] real part $\sigma_1(\omega)$ and [B] imaginary part $\sigma_2(\omega)$ with GGA+*U*.

4. Conclusions

In summary, this study's conclusions are as follows:

Edelweiss Applied Science and Technology
ISSN: 2576-8484
Vol. 8, No. 6: 413-430, 2024
DOI: 10.55214/25768484.v8i6.2093

(1) Ferromagnetic bcc is determined to be the stable ground state for the Fe atom in both GGA and GGA+U simulations. Our findings are consistent with other research (3, 5, 47, 59, 77), which is strongly related to the crystal structure.
(2) For the NM, FM, and AFM states of bcc and fcc Fe with GGA and GGA+U calculations, the equilibrium atomic volume Vo, lattice constant a, and atomic energy E at equilibrium volume clearly demonstrate that our results are pretty realistic when compared with other results of prior studies (50 – 52).
(3) Our study cases for both GGA and GGA+U calculations show that the zero-pressure bulk modulus B_0, its pressure derivative B'_0, and the magnetic moments (μ) agree well with experimental data and previous all-electron calculations (5, 54, 56), with the magnetic moment per unit cell increasing upon including strong correlations. In comparison to other outcomes, the GGA also yields results that are rather plausible (53, 56 – 58). Improved agreement with experiments and other theoretical investigations is seen from our GGA results, which significantly outperform previous DFT results.
(4) For all GGA and GGA+U computations, the DOS varies significantly with the FM state but not much with the NM or AFM states. This is consistent with IoTa's findings (1) and related theoretical work (5, 24). For our PDOS calculations using GGA and GGA+U for the NM, FM, and AFM states for bcc and fcc Fe. An antiferromagnetic state eliminates the instability caused by the high density of states at the Fermi energy; this outcome is in excellent agreement with that stated in Ref (66).
(5) The optical properties obtained for bcc and fcc Fe for NM, FM, and AFM states with GGA and GGA+U are similar to those of previous studies (15, 73). These results include the interband dielectric function $\varepsilon(\omega)$, variation in the energy-loss spectrum $L(\omega)$, absorption coefficient $\alpha(\omega)$, refractive index $n(\omega)$, reflectivity $R(\omega)$, and optical absorption $\sigma(\omega)$.

Acknowledgements:
The Researchers would like to thank the Deanship of Graduate Studies and Scientific Research at Qassim University for financial support (QU-APC-2024-9/1).

References

[1] Iota, V., et al., Electronic structure and magnetism in compressed 3d transition metals. Applied Physics Letters, 2007. 90(4). DOI: 10.1063/1.2434184.
[2] Motizuki, K., et al., Electronic structure and magnetism of 3d-transition metal pnictides. 2010. DOI: 10.1007/978-3-642-03420-6.
[3] Ishimatsu, N., et al., Stability of ferromagnetism in Fe, Co, and Ni metals under high pressure. Journal of the Physical Society of Japan, 2007. 76(6): p. 064703-064703. https://doi.org/10.1143/jpsj.76.064703
[4] Moruzzi, V., P. Marcus, and P. Pattnaik, Magnetic transitions in bcc vanadium, chromium, manganese, and iron. Physical Review B, 1988. 37(14): p. 8003. https://doi.org/10.1103/PhysRevB.37.8003.
[5] Mohammed, Y.S., et al., Stability of ferromagnetism in Fe, Co, and ni metals under high pressure with GGA and GGA+ U. Journal of magnetism and magnetic materials, 2010. 322(6): p. 653-657. https://doi.org/10.1016/j.jmmm.2009.10.033.
[6] Torchio, R., O. Mathon, and S. Pascarelli, XAS and XMCD spectroscopies to study matter at high pressure: probing the correlation between structure and magnetism in the 3d metals. Coordination Chemistry Reviews, 2014. 277: p. 80-94. https://doi.org/10.1016/j.ccr.2014.02.024.
[7] Soulairol, R., C.-C. Fu, and C. Barreteau, Structure and magnetism of bulk Fe and Cr: from plane waves to LCAO methods. Journal of Physics: Condensed Matter, 2010. 22(29): p. 295502. DOI 10.1088/0953-8984/22/29/295502.
[8] Janak, J., A. Williams, and V. Moruzzi, Self-consistent band theory of the Fermi-surface, optical, and photoemission properties of copper. Physical Review B, 1975. 11(4): p. 1522. https://doi.org/10.1103/PhysRevB.11.1522.

[9] Blaha, P., et al., WIEN2k, An Augmented Plane Wave Plus Local Orbitals Program for Calculating Crystal Properties (Vienna University of Technology, Austria, 2001).

[10] Hubbard, J., The magnetism of iron. Physical Review B, 1979. 19(5): p. 2626. https://doi.org/10.1103/PhysRevB.19.2626.

[11] You, M., et al., Magnetism in iron at high temperatures. Physical Review Letters, 1980. 44(19): p. 1282. https://doi.org/10.1103/PhysRevLett.44.1282.

[12] Boulard, E., et al., Experimental investigation of the stability of Fe-rich carbonates in the lower mantle. Journal of Geophysical Research: Solid Earth, 2012. 117(B2). https://doi.org/10.1029/2011JB008733.

[13] Stein, F., G. Sauthoff, and M. Palm, Experimental determination of intermetallic phases, phase equilibria, and invariant reaction temperatures in the Fe-Zr system. Journal of Phase Equilibria, 2002. 23(6): p. 480-494.

[14] Chen, T., et al., Experimental investigation and thermodynamic assessment of the Fe-Pr and Fe-Nd binary systems. Calphad, 2016. 55: p. 270-280. https://doi.org/10.1016/j.calphad.2016.10.004.

[15] Menéndez, J.L., et al., Optical and magneto-optical properties of Fe nanoparticles. Physical Review B, 2002. 65(20): p. 205413. https://doi.org/10.1103/PhysRevB.65.205413.

[16] Antonov, V., et al., Lasing and luminescence characteristics of Fe: CdTe single crystal at room temperature. Optical Materials, 2023. 139: p. 113768. https://doi.org/10.1016/j.optmat.2023.113768.

[17] Kortright, J.B. and S.-K. Kim, Resonant magneto-optical properties of Fe near its 2 p levels: Measurement and applications. Physical Review B, 2000. 62(18): p. 12216. https://doi.org/10.1103/PhysRevB.62.12216.

[18] Tiago, M.L., et al., Evolution of magnetism in iron from the atom to the bulk. 2006. 97(14): p. 147201. https://doi.org/10.1103/PhysRevLett.97.147201.

[19] Ma, P.-W., C. Woo, and S. Dudarev, High-temperature dynamics of surface magnetism in iron thin films. Philosophical Magazine, 2009. 89(32): p. 2921-2933. https://doi.org/10.1080/14786430903130854.

[20] Schlage, K., et al., The formation and magnetism of iron nanostructures on ordered polymer templates. New Journal of Physics, 2012. 14(4): p. 043007. DOI 10.1088/1367-2630/14/4/043007.

[21] Zeng, Z.-Y., et al., Magnetism and phase transitions of iron under pressure. Journal of Physics: Condensed Matter, 2008. 20(42): p. 425217. DOI 10.1088/0953-8984/20/42/425217.

[22] Weaver, J.H., et al., Optical properties of metals. Applied optics, 1981. 20(7): p. 1124_1-1125. https://doi.org/10.1364/AO.20.1124_1.

[23] Poulin, B.A., et al., Effects of iron on optical properties of dissolved organic matter. 2014. 48(17): p. 10098-10106.

[24] Kubo, Y. and S. Wakoh, Optical Properties of 3d Transition Metals: V, Cr, Fe and Ni. Journal of the Physical Society of Japan, 1981. 50(3): p. 835-842. https://doi.org/10.1143/JPSJ.50.835.

[25] Moradian, R., et al., Structural, magnetic, electronic and optical properties of iron cluster (Fe6) decorated boron nitride sheet. Physica E: Low-dimensional Systems and Nanostructures, 2012. 46: p. 182-188. https://doi.org/10.1016/j.physe.2012.08.012.

[26] Dadashi, S., R. Poursalehi, and H. Delavari, Structural and optical properties of pure iron and iron oxide nanoparticles prepared via pulsed Nd: YAG laser ablation in liquid. Procedia materials science, 2015. 11: p. 722-726. https://doi.org/10.1016/j.mspro.2015.11.052.

[27] Petersen, M., et al., Improving the efficiency of FP-LAPW calculations. Computer Physics Communications, 2000. 126(3): p. 294-309. https://doi.org/10.1016/S0010-4655(99)00495-6.

[28] Kresse, G. and D. Joubert, From ultrasoft pseudopotentials to the projector augmented-wave method. Physical review b, 1999. 59(3): p. 1758. https://doi.org/10.1103/PhysRevB.59.1758.

[29] Bagayoko, D., Understanding density functional theory (DFT) and completing it in practice. AIP Advances, 2014. 4(12): p. 127104. https://doi.org/10.1063/1.4903408.

[30] Perdew, J.P., K. Burke, and M. Ernzerhof, Generalized gradient approximation made simple. Physical review letters, 1996. 77(18): p. 3865. https://doi.org/10.1103/PhysRevLett.77.3865.

[31] Tran, F., WIEN2k: an augmented plane wave plus local orbitals program for calculating crystal properties. 2018. http://hdl.handle.net/20.500.12708/100909.

[32] Schwarz, K., P. Blaha, and G.K. Madsen, Electronic structure calculations of solids using the WIEN2k package for material sciences. Computer physics communications, 2002. 147(1-2): p. 71-76. https://doi.org/10.1016/S0010-4655(02)00206-0.

[33] Blaha, P., et al., WIEN2k, An Augmented Plane Wave-Local Orbitals Program for Calculating Crystal Properties revised edition June 2002, Univ Prof. Dr. Karlheinz Schwarz Technische Universität Wien, Institut für Physikalische und Theoretische Chemie, Getreidemarkt, 2002. 9: p. 156.

[34] Zhang, Z., Y. Sun, and R.M. Wentzcovitch, PBE-GGA Predicts the B8 ↭ B2 Phase Boundary of FeO at Earth's Core Conditions. arXiv preprint arXiv:2211.15052, 2022. https://doi.org/10.48550/arXiv.2211.15052.

[35] Johnson, K.A. and N. Ashcroft, Corrections to density-functional theory band gaps. Physical Review B, 1998. 58(23): p. 15548. https://doi.org/10.1103/PhysRevB.58.15548.

[36] Dudarev, S.L., et al., Electron-energy-loss spectra and the structural stability of nickel oxide: An LSDA+*U* study. Physical Review B, 1998. 57(3): p. 1505. https://doi.org/10.1103/PhysRevB.57.1505.

[37] Petukhov, A., et al., Correlated metals and the LDA+ U method. Physical Review B, 2003. 67(15): p. 153106. https://doi.org/10.1103/PhysRevB.67.153106.
[38] Monkhorst, H.J. and J.D. Pack, Special points for Brillouin-zone integrations. Physical review B, 1976. 13(12): p. 5188. https://doi.org/10.1103/PhysRevB.13.5188.
[39] Wang, Q.-B., et al., A GGA+*U* study of the optical properties of vanadium doped ZnO with and without single intrinsic vacancy. Optics Communications, 2013. 297: p. 79-84. https://doi.org/10.1016/j.optcom.2013.01.073.
[40] Pack, J.D. and H.J. Monkhorst, "Special points for Brillouin-zone integrations"—a reply. Physical Review B, 1977. 16(4): p. 1748. https://doi.org/10.1103/PhysRevB.16.1748.
[41] Mustafa, G., et al., Electronic and magnetic properties of BaUO3 by modified Becke–Johnson (mBJ) functional. Modern Physics Letters B, 2018. 32(15): p. 1850164. https://doi.org/10.1142/S0217984918501646.
[42] Methfessel, M. and A. Paxton, High-precision sampling for Brillouin-zone integration in metals. Physical Review B, 1989. 40(6): p. 3616. https://doi.org/10.1103/PhysRevB.40.3616.
[43] Blöchl, P.E., Projector augmented-wave method. Physical review B, 1994. 50(24): p. 17953. https://doi.org/10.1103/PhysRevB.50.17953.
[44] Birch, F., The effect of pressure upon the elastic parameters of isotropic solids, according to Murnaghan's theory of finite strain. Journal of Applied Physics, 1938. 9(4): p. 279-288. https://doi.org/10.1063/1.1710417.
[45] Katsura, T. and Y. Tange, A simple derivation of the Birch–Murnaghan equations of state (EOSs) and comparison with EOSs derived from other definitions of finite strain. Minerals, 2019. 9(12): p. 745. https://doi.org/10.3390/min9120745.
[46] Tyuterev, V. and N. Vast, Murnaghan's equation of state for the electronic ground state energy. Computational materials science, 2006. 38(2): p. 350-353. https://doi.org/10.1016/j.commatsci.2005.08.012.
[47] Moruzzi, V., Singular volume dependence of transition-metal magnetism. Physical review letters, 1986. 57(17): p. 2211. https://doi.org/10.1103/PhysRevLett.57.2211.
[48] Moruzzi, V. and P. Marcus, Magnetism in bcc 3 d transition metals. Journal of applied physics, 1988. 64(10): p. 5598-5600. https://doi.org/10.1063/1.342293.
[49] Krasko, G.L. and G.B.J.P.R.B. Olson, Energetics of bcc-fcc lattice deformation in iron. 1989. 40(17): p. 11536. https://doi.org/10.1103/PhysRevB.40.11536.
[50] Guo, G. and H.J.C.J.o.P. Wang, Gradient-corrected density functional calculation of elastic constants of Fe, Co and Ni in bcc, fcc and hcp structures. 2000. 38(5): p. 949-961.
[51] Kittel, C., Introduction to solid state physics. 2005: John Wiley & sons, inc.
[52] Pham, H.H., T.J.C. Cagin, Materials, and Continua, Lattice dynamics and second and third order elastic constants of iron at elevated pressures. 2010. 16(1): p. 175.
[53] Jiang, D. and E.A.J.P.R.B. Carter, Carbon dissolution and diffusion in ferrite and austenite from first principles. 2003. 67(21): p. 214103. https://doi.org/10.1103/PhysRevB.67.214103.
[54] Jephcoat, A.P., H. Mao, and P.M.J.J.o.G.R.S.E. Bell, Static compression of iron to 78 GPa with rare gas solids as pressure-transmitting media. 1986. 91(B5): p. 4677-4684. https://doi.org/10.1029/JB091iB05p04677.
[55] Wang, C., B. Klein, and H.J.P.r.l. Krakauer, Theory of magnetic and structural ordering in iron. 1985. 54(16): p. 1852. https://doi.org/10.1103/PhysRevLett.54.1852.
[56] Gough, C., Introduction to Solid State Physics (6th edn). 1986, IOP Publishing. DOI 10.1088/0031-9112/37/11/034.
[57] Lee, D.-K. and S.-C.J.J.o.M. Hong, Correlation between structures and magnetism in iron: ferromagnetism and antiferromagnetism. 2007. 12(2): p. 68-71. https://doi.org/10.4283/JMAG.2007.12.2.068.
[58] Acet, M., et al., High-temperature moment-volume instability and anti-Invar of γ-Fe. 1994. 49(9): p. 6012. https://doi.org/10.1103/PhysRevB.49.6012.
[59] Singh, D., W. Pickett, and H.J.P.R.B. Krakauer, Gradient-corrected density functionals: Full-potential calculations for iron. 1991. 43(14): p. 11628. https://doi.org/10.1103/PhysRevB.43.11628.
[60] Stojić, N., N.J.J.o.m. Binggeli, and m. materials, Phase stability of Fe and Mn within density-functional theory plus on-site Coulomb interaction approaches. 2008. 320(3-4): p. 100-106. https://doi.org/10.1016/j.jmmm.2007.05.011.
[61] Leung, T.-C., C.T. Chan, and B.N.J.P.R.B. Harmon, Ground-state properties of Fe, Co, Ni, and their monoxides: Results of the generalized gradient approximation. 1991. 44(7): p. 2923. https://doi.org/10.1103/PhysRevB.44.2923.
[62] Cho, J.-H. and M.J.P.R.B. Scheffler, Ab initio pseudopotential study of Fe, Co, and Ni employing the spin-polarized LAPW approach. 1996. 53(16): p. 10685. https://doi.org/10.1103/PhysRevB.53.10685.
[63] Cococcioni, M. and S.J.P.R.B. De Gironcoli, Linear response approach to the calculation of the effective interaction parameters in the LDA+ U method. 2005. 71(3): p. 035105. https://doi.org/10.1103/PhysRevB.71.035105.
[64] Lew, A., et al., Quantum mechanics based multiscale modeling of stress-induced phase transformations in iron. 2006. 54(6): p. 1276-1303. https://doi.org/10.1016/j.jmps.2005.11.009.
[65] Abrahams, S., L. Guttman, and J.J.P.R. Kasper, Neutron diffraction determination of antiferromagnetism in face-centered cubic (γ) iron. 1962. 127(6): p. 2052. https://doi.org/10.1103/PhysRev.127.2052.
[66] Mohammed, Y.S., et al., STABILITY AND OPTICAL PROPERTIES OF VANADIUM WITH GGA AND GGA+ U CALCULATIONS. 2023.

[67] Ajmad, I., B. amin, M. Maqbool, S. Muhammad, G. Murtaza, S. Ali, A. Noor. Optoelectronic Response of $GeZn_2O_4$ through the Modified Becke—Johnson Potential, Chin. Phys. Lett, 2012. 29: p. 097102. DOI 10.1088/0256-307X/29/9/097102.
[68] Wooten, F., Optical Properties of Solids Academic Press: New York. NY, USA, London, UK, 1972.
[69] Bekhti-Siad, A., et al., Electronic, optical and thermoelectric investigations of Zintl phase AE3AlAs3 (AE= Sr, Ba): first-principles calculations. 2018. 56(3): p. 870-879. https://doi.org/10.1016/j.cjph.2018.03.022.
[70] Vu, T.V., et al., Theoretical prediction of electronic, transport, optical, and thermoelectric properties of Janus monolayers In 2 X O (X= S, Se, Te). 2021. 103(8): p. 085422. https://doi.org/10.1103/PhysRevB.103.085422.
[71] Shinotsuka, H., et al., First-principles Calculations of Optical Energy Loss Functions for 30 Compound and 5 Elemental Semiconductors. 2021. 19: p. 70-87. https://doi.org/10.1380/ejssnt.2021.70.
[72] Johnson, P. and R. Christy, Optical constants of transition metals: Ti, V, Cr, Mn, Fe, Co, Ni, and Pd. Physical review B, 1974. 9(12): p. 5056. https://doi.org/10.1103/PhysRevB.9.5056.
[73] John, R., S.J.C.s.t. Padmavathi, and applications, Ab initio calculations on structural, electronic and optical properties of ZnO in wurtzite phase. 2016. 5(02): p. 24.
[74] Romaniello, P., et al., Optical properties of bcc transition metals in the range 0–40 eV. 2006. 73(7): p. 075115. https://doi.org/10.1103/PhysRevB.73.075115.
[75] Rai, D., et al., Electronic and optical properties of cubic SrHfO3 at different pressures: a first principles study. 2017. 186: p. 620-626.
[76] Fox, M., Optical properties of solids. Vol. 3. 2010: Oxford university press.
[77] Krasko, G.L. and G.J.J.o.a.p. Olson, Ferromagnetism and crystal lattice stability of bcc and fcc iron. 1990. 67(9): p. 4570-4572. https://doi.org/10.1063/1.344873.